Nuclear Inst. and Methods in Physics Research, A 1018 (2021) 165828

Contents lists available at ScienceDirect

Nuclear Inst. and Methods in Physics Research, A

journal homepage: www.elsevier.com/locate/nima

Combined analysis of HPK 3.1 LGADs using a proton beam, beta source, and probe station towards establishing high volume quality control

R. Heller [a,*], A. Abreu [c], A. Apresyan [a], R. Arcidiacono [f,h], N. Cartiglia [f], K. DiPetrillo [a], M. Ferrero [f], M. Hussain [a], M. Lazarovitz [c], H. Lee [d], S. Los [a], C.S. Moon [d], C. Peña [a,b], F. Siviero [g], V. Sola [f], T. Wamorkar [e], S. Xie [b]

[a] Fermi National Accelerator Laboratory, Batavia, IL, USA
[b] California Institute of Technology, Pasadena, CA, USA
[c] University of Kansas, KS, USA
[d] Kyungpook National University, Daegu, South Korea
[e] Northeastern University, MA, USA
[f] INFN, Torino, Italy
[g] Università di Torino, Torino, Italy
[h] Università del Piemonte Orientale, Italy

ARTICLE INFO

Keywords:
Silicon
Timing
LGAD
Test beam
Beta source

ABSTRACT

The upgrades of the CMS and ATLAS experiments for the high luminosity phase of the Large Hadron Collider will employ precision timing detectors based on Low Gain Avalanche Detectors (LGADs). We present a suite of results combining measurements from the Fermilab Test Beam Facility, a beta source telescope, and a probe station, allowing full characterization of the HPK type 3.1 production of LGAD prototypes developed for these detectors. We demonstrate that the LGAD response to high energy test beam particles is accurately reproduced with a beta source. We further establish that probe station measurements of the gain implant accurately predict the particle response and operating parameters of each sensor, and conclude that the uniformity of the gain implant in this production is sufficient to produce full-sized sensors for the ATLAS and CMS timing detectors.

1. Introduction

Future colliders, including the high luminosity upgrade of the Large Hadron Collider (HL-LHC) at CERN, will operate with instantaneous luminosities at least five times higher than in current LHC running conditions. The rise in instantaneous luminosity will increase the rate of simultaneous interactions per bunch crossing (pileup) to approximately 200 at the HL-LHC [1], and up to 1,200 at the FCC-hh [2]. The large amount of pileup exacerbates the difficulties in separating particles that originate from the interaction of interest from those produced in pileup interactions. Precision timing has been identified as a pileup mitigation technique to complement precision tracking at the HL-LHC. Pileup interactions are spread over a period of approximately 200 ps, and a time measurement with precision of approximately 30–40 ps will reduce the effective rate of pileup by a factor of five, yielding pileup levels comparable with current LHC conditions. In this paper, we report results of measurements with thin low-gain avalanche detectors (LGADs), which will be used in the CMS and ATLAS upgrades for HL-LHC [3] and have been demonstrated to achieve time resolutions below 30 ps [4–6].

Previous measurements of LGAD sensor performance have focused on small, mm scale devices with few pads. The CMS timing detector will be constructed of larger area sensors ($2 \times 4\,\mathrm{cm}^2$). Effective operation of such large sensors will require highly uniform gain layer deposition to enable the required response across the sensor area constrained to a single operating voltage. The ability to produce uniform LGAD wafers is thus a key requirement for a successful timing detector. The measurements presented in this paper are among the first to explicitly address this scalability requirement.

In this paper, we follow several approaches to study the LGAD batch produced in 2018 by Hamamatsu, hereafter referred to as HPK type 3.1 LGADs. Enabled by the development of a 16-channel readout board at Fermilab, we demonstrate for the first time the successful operation of a large, 16-pad LGAD sensor using 120 GeV protons at the Fermilab Test Beam Facility (FTBF). These measurements demonstrate that an HPK type 3.1 LGAD sensor that meets the uniformity in efficiency, gain, and time resolution that are required for the CMS and ATLAS timing detectors. Furthermore, we demonstrate that the size of the inactive interpad-gap regions measured by a laser using the transient current

* Corresponding author.
E-mail address: rheller@fnal.gov (R. Heller).

https://doi.org/10.1016/j.nima.2021.165828
Received 3 April 2021; Received in revised form 20 July 2021; Accepted 13 September 2021
Available online 23 September 2021
0168-9002/Published by Elsevier B.V.

technique (TCT) is consistent with the measurement using the proton beam.

We then establish that sensor characterization based on a Ruthenium-106 beta source yields results consistent with those from the proton beam. This conclusion enables the use of the beta source setup to perform studies of sensor uniformity on scales across the entire wafer. These high-volume studies would not be feasible with the proton beam alone, due to the limited availability of beamtime. Our measurements demonstrate that the gain uniformity across the HPK type 3.1 LGAD wafer meets the requirements of the CMS and ATLAS timing detectors.

Finally, by comparing beta source measurements with probe station measurements of the gain implant in each sensor, we establish a clear linear relationship between the operational bias voltage and the gain layer depletion voltage. This observation allows reliably predicting the gain of the sensor from probe station capacitance–voltage (CV) measurements, therefore enhancing the power of the probe station as a tool for studying wafer-scale uniformity. As a result, we show that the probe station can be used as a fast and reliable way to establish sensor quality control during the production phase of the CMS and ATLAS timing detectors. A similar correspondence between the gain layer depletion voltage and the operating voltage has been established for wide variation between distinct sensor designs [7]. In contrast, the results shown here probe this relationship with a larger sensor population, and focus on variation within the manufacturing tolerance for the context of production quality control.

The paper is organized as follows: the LGAD sensors are discussed in Section 2; the experimental setups are described in Section 3; the test beam measurements are reported in Section 4; the beta source setup results and the correspondence with probe measurements are presented in Section 5; and the conclusions are given in Section 6.

2. LGAD sensors under study

LGAD sensors are produced by introducing an additional layer of p^+ material (e.g. Boron) close to the n–p junction of traditional silicon sensors. This results in a very high electric field in the region within a depth of a few micrometers of the junction. This region is referred to as the "gain" or "multiplication" layer. The initial signal generated by the MIP ionization is amplified through an avalanche process initiated by an electron or a hole accelerating through the gain region. The amplified signals maintain fast slew rate, resulting in excellent timing characteristics [4]. Signals are read out from the n^+ cathode. Since the bulk material is a high resistivity p-type silicon, a shallow uniform p-spray doping is usually implemented to isolate the cathodes. To reduce the magnitude of the electric field at the perimeter of each signal pad, an additional deep n^+ doping region (Junction Terminating Extension or JTE) is implemented. JTEs are characteristic feature of LGAD sensors, and results in regions of no gain between pads, referred to in the following as the "inter-pad gap".

In this paper we present studies of the new HPK type 3.1 LGAD sensors, designed to achieve increased radiation tolerance compared to previous LGADs. With a deeper gain implant and generally steeper onset of gain as a function of bias voltage, the HPK 3.1 LGADs can be operated at relatively low bias voltage before irradiation. The bias voltage can then be increased progressively to compensate for the gain-loss due to the acceptor removal that occurs during irradiation, which also increases the breakdown voltage.

The HPK type 3.1 LGADs were produced with a variety of specifications. The LGADs were produced in 6-inch wafers, comprised of sensors of different geometries as shown in Fig. 1. The sensors are composed of different grid arrangements of "pads", which are electrically isolated from each other and read out separately. The sensors studied in this paper are summarized in Table 1.

Each sensor has a variety of inter-pad separation ranging between 30 µm to 100 µm. Some sensors were produced with complete metalization coverage and some with mostly non-metalized open surfaces.

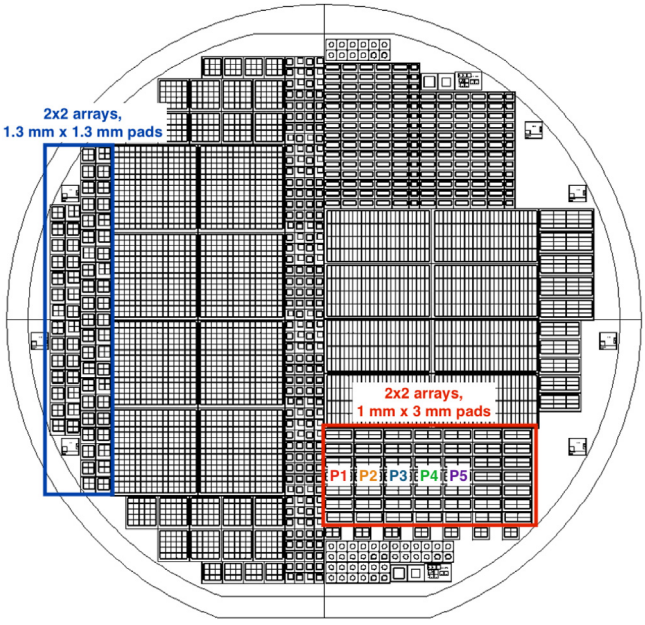

Fig. 1. HPK 3.1 wafer layout. The blue and red boxes indicate the regions of the wafer populated with 2 × 2 arrays with $1.3 \times 1.3\,mm^2$ and $1 \times 3\,mm^2$ pad sizes, respectively. The labels P1–P5 indicate columns of sensors tracked within the population of $1 \times 3\,mm^2$ sensors. (For interpretation of the references to color in this figure legend, the reader is referred to the web version of this article.)

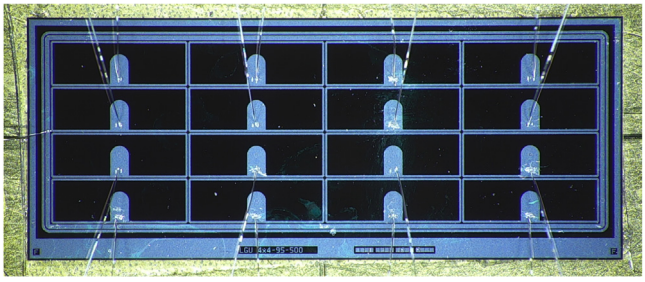

Fig. 2. HPK type 3.1 4x4 multi-pad sensor with pad size $1 \times 3\,mm^2$) and a non-metalized surface.

Previous studies with metalized and non-metalized LGADs [6] have observed differences in signal propagation time and radiation hardness. A characterization campaign for sensors spanning the full range of parameters described above is presented in this paper.

The HPK type 3.1 wafer layout is shown in Fig. 1. Each wafer was split in half, with multi-pad sensor arrays of pad size $1.3 \times 1.3\,mm^2$ on the left, and $1 \times 3\,mm^2$ on the right. The CMS and ATLAS timing detectors will employ LGADs with a pad size of $1.3 \times 1.3\,mm^2$.

The test beam measurements described in this paper focus on a detailed study of a non-metalized 4 x 4 multi-pad sensor with $1 \times 3\,mm^2$ pad size and 95 µm inter-pad gap. A photo of this sensor is shown in Fig. 2. Additionally, several similar 2 x 2 multi-pad sensors were studied spanning a variation in the inter-pad spacing from 30 µm to 95 µm. Example photos of these sensors can be seen in Fig. 3. Since these sensors are typically studied on single channel readout boards (described in Section 3.1), the three unread pads are grounded via connection to the sensor guard ring.

The beta source telescope, described in Section 3.4 allows for testing a significantly higher volume of sensors thanks to much greater availability and ease of access than the test beam. This paper describes a campaign that characterized a sample of 22 sensors and documented the variation of the performance metrics using signals from ionizing particles. The campaign used a set of 2 x 2 multi-pad sensors with pad

Table 1
Summary of all the sensors included in the studies described in this paper. The first two blocks list the sensors with pad size $1 \times 3\,\text{mm}^2$ and $1.3 \times 1.3\,\text{mm}^2$ used in the beta source measurements described in Section 5. The third block lists the sensors used in the test beam measurements described in Section 4.

Sensor label	Pad arrangement	Fully metalized	Interpad gap	Pad size
P1 50 µm	2 × 2	No	50 µm	$1 \times 3\,\text{mm}^2$
P2 95 µm	2 × 2	No	95 µm	$1 \times 3\,\text{mm}^2$
P2 95 µm (metal)	2 × 2	Yes	95 µm	$1 \times 3\,\text{mm}^2$
P2 50 µm	2 × 2	No	50 µm	$1 \times 3\,\text{mm}^2$
P3 95 µm	2 × 2	No	95 µm	$1 \times 3\,\text{mm}^2$
P3 95 µm (metal)	2 × 2	Yes	95 µm	$1 \times 3\,\text{mm}^2$
P3 50 µm	2 × 2	No	50 µm	$1 \times 3\,\text{mm}^2$
P4 95 µm	2 × 2	No	95 µm	$1 \times 3\,\text{mm}^2$
P4 95 µm (metal)	2 × 2	Yes	95 µm	$1 \times 3\,\text{mm}^2$
P4 50 µm	2 × 2	No	50 µm	$1 \times 3\,\text{mm}^2$
P5 95 µm (metal)	2 × 2	Yes	95 µm	$1 \times 3\,\text{mm}^2$
90 µm #1	2 × 2	No	90 µm	$1.3 \times 1.3\,\text{mm}^2$
90 µm #2	2 × 2	No	90 µm	$1.3 \times 1.3\,\text{mm}^2$
90 µm (metal) #1	2 × 2	Yes	90 µm	$1.3 \times 1.3\,\text{mm}^2$
90 µm (metal) #2	2 × 2	Yes	90 µm	$1.3 \times 1.3\,\text{mm}^2$
90 µm (metal) #3	2 × 2	Yes	90 µm	$1.3 \times 1.3\,\text{mm}^2$
90 µm (metal) #4	2 × 2	Yes	90 µm	$1.3 \times 1.3\,\text{mm}^2$
90 µm (metal) #5	2 × 2	Yes	90 µm	$1.3 \times 1.3\,\text{mm}^2$
50 µm (metal) #1	2 × 2	Yes	50 µm	$1.3 \times 1.3\,\text{mm}^2$
50 µm (metal) #2	2 × 2	Yes	50 µm	$1.3 \times 1.3\,\text{mm}^2$
30 µm (metal) #1	2 × 2	Yes	30 µm	$1.3 \times 1.3\,\text{mm}^2$
30 µm (metal) #2	2 × 2	Yes	30 µm	$1.3 \times 1.3\,\text{mm}^2$
4 × 4 95 µm	4 × 4	No	95 µm	$1 \times 3\,\text{mm}^2$
30 µm	2 × 2	No	30 µm	$1 \times 3\,\text{mm}^2$
50 µm	2 × 2	No	50 µm	$1 \times 3\,\text{mm}^2$
70 µm	2 × 2	No	70 µm	$1 \times 3\,\text{mm}^2$

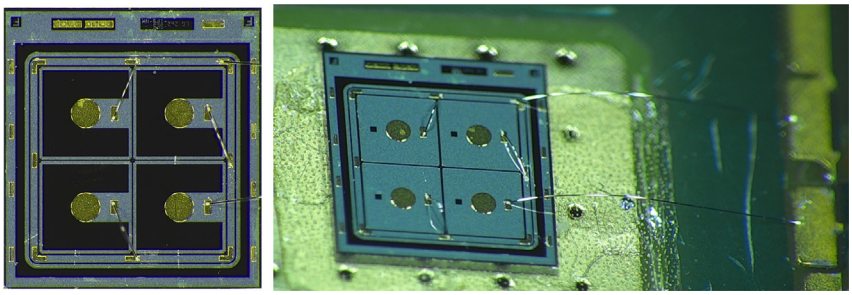

Fig. 3. HPK type 3.1 2x2 multi-pad sensor of pad size $1.3 \times 1.3\,\text{mm}^2$) without metalized surface (left) and with fully metalized surface (right).

sizes of ($1.3 \times 1.3\,\text{mm}^2$ and $1 \times 3\,\text{mm}^2$), spanning the full range of inter-pad gaps, and including both metalized and non-metalized sensors. The design parameters of all 22 sensors can be found in Table 1. Prior to the beta source telescope measurements, all of these sensors were characterized with capacitance–voltage (CV) measurements using a probe station in the Torino UFSD lab. For the sensors with $1 \times 3\,\text{mm}^2$ pad size, it was possible to trace the provenance to the approximate position on the wafer itself, as indicated in Fig. 1. The locations on wafer were not preserved after dicing for the sensors with $1.3 \times 1.3\,\text{mm}^2$ pad size.

3. Experimental setup

3.1. LGAD readout boards

The test beam and beta source measurements make use of two specialized readout boards: the single-channel UCSC board, optimized for time resolution measurements; and the 16-channel FNAL board, which enables simultaneous readout of more sensor pads.

The UCSC board is based on a single amplification stage which provides a very clean single-channel measurement. A 470 Ω transimpedance amplifier with an analog bandwidth of 1.6 GHz is used, with very low noise, due to extensive shielding and isolation [4]. In all measurements described in this paper, the UCSC board is supplemented with an additional stage of amplification provided by a Mini-Circuits GALI-52+ evaluation board, resulting in a total transimpedance of approximately 5 kΩ. Several copies of the UCSC board (v1.4) were used and found to have excellent inter-board uniformity, as described in Section 5.2. The 16-channel FNAL board enables readout of large multi-pad LGAD sensors with sizes up to $26.5 \times 11.5\ \text{mm}^2$. Each readout channel is amplified by two amplifier stages based on the Mini-Circuits GALI-66+ integrated circuit. In this particular configuration, the amplifiers used a 25 Ω input impedance, for a total transimpedance of approximately 5 kΩ and a bandwidth of 1 GHz. The amplifier chain of each readout channel is found to have uniform gain with approximately 10% variation from channel to channel.

In general, the UCSC board is able to provide a better time resolution measurement for a single pad, while the 16-channel board affords the ability to study multi-channel sensors with a time resolution that is slightly degraded.

3.2. Experimental chambers and data acquisition

For all test beam, beta source, and laser measurements, the LGADs were mounted inside similar experimental chambers that provide controlled environments and enable stable, reproducible results. Inside the chambers, the sensors and read-out boards were coupled to aluminum cooling blocks shown on Fig. 5, which are mounted on a remotely

operated motorized stage. The cooling blocks are machined with a dense network of cooling channels that ensure efficient cooling of the mounted electronics. A chilled glycol–water solution circulated through the cooling blocks, capable of holding the sensors at constant temperatures ranging from −20 °C to +22 °C, as verified with on-board thermistors. Particularly important for the higher-power 16-channel board, direct contact with the cooling blocks enables significantly more heat dissipation than possible with cooling via contact with cold air alone. All relevant sensor operational parameters were continuously monitored and recorded, including the sensor temperature via on-board thermistors, the sensor bias voltage and leakage current, and the temperature and humidity of the air. These values were subsequently synchronized and combined with the signal waveform data. The temperature of the readout boards were found to be stable to within 0.1 °C. The relative humidity of the environmental chamber was kept to less than 10% by means of a constant flow of nitrogen gas.

For both the test beam and the beta source measurements, a precise reference time stamp is provided by a Photek 240 micro-channel plate (MCP-PMT) detector, placed inside the environmental chambers just behind the LGADs [8]. Cherenkov radiation emitted by protons or beta particles traversing the glass window produce photoelectrons that generate a large, steeply rising MCP-PMT signal. The time resolution of the MCP-PMT response to protons in the test beam was measured to be better than 10 ps by comparing timestamps produced by two Photek 240 MCP-PMTs aligned in the beamline at once. Due to the lower intensity of Cherenkov radiation emitted by beta particles, the MCP-PMT signals in the beta setup have smaller amplitudes, resulting in a time resolution of approximately 15 ps, as described in Section 5.1.

The LGAD and MCP-PMT waveforms were acquired using a Keysight MSOX92004 A 4-channel oscilloscope [9], which provides digitized waveforms sampled at 20–40 GS/s, and the oscilloscope bandwidth was set to 2 GHz.

3.3. Fermilab test beam facility experiment

The test beam measurements were performed at the FTBF [10], which provides a unique environment to characterize prototype detectors for collider experiments. The FTBF uses the 120 GeV proton beam from the Fermilab Main Injector accelerator. The FTBF beam is resonantly extracted in a slow spill for each Main Injector cycle delivering a single 4.2 s long spill per minute, tuned to yield approximately 100,000 protons in each spill. The primary beam of 120 GeV protons is bunched at 53 MHz. The beam size can be tuned to obtain widths from 2-3 mm up to approximately 1 cm. All measurements presented in this paper were taken with such primary beam particles.

The FTBF is equipped with a silicon tracking telescope to measure the position of each incident proton [11]. The telescope consists of four pixel layers with cell size $100 \times 150\,\mu m^2$, and fourteen strip modules with 60 μm pitch, in alternating orthogonal directions in the plane orthogonal to the beam axis. The LGAD chamber was placed approximately 2 m downstream from the center of the telescope. To detect and reject protons that scatter in any material along the beam line, two of the fourteen strip layers are located immediately downstream of the LGAD chamber. During this data-taking period, the resolution of the telescope spatial measurement at the LGAD position was approximately 50 μm, somewhat degraded with respect to its nominal resolution of 10–15μm due to the long extrapolation from the telescope and from the material along the beamline. The FTBF tracker setup and the LGAD environmental chamber can be seen in Fig. 4.

The telescope data acquisition hardware is based on the CAPTAN (Compact And Programmable daTa Acquisition Node) system developed at Fermilab. The CAPTAN is a flexible and versatile data acquisition system designed to meet the readout and control demands of a variety of pixel and strip detectors for high energy physics applications [12].

The trigger signal to both the telescope and the oscilloscope originates in an independent scintillator coupled to a photomultiplier tube. The telescope and oscilloscope data are merged offline by matching trigger counters from each system.

The Keysight MSOX92004 oscilloscope's extremely deep memory and segmented acquisition mode is particularly well suited for the FTBF beam structure, allowing a burst of 50,000 events to be acquired during each 4.2 s spill and written to disk during the longer inter-spill period. To efficiently read the multi-pad sensors using only three channels on the oscilloscope, multiple readout channels are connected to a high performance 20 GHz RF switch [13]. Then, the signals from different sensor pads can be remotely selected as input to the oscilloscope for readout without interrupting the beam.

The data acquisition and reconstruction process is managed by an automated software framework known as JARVIS [14]. This framework synchronizes the operation of the oscilloscope, telescope, and any other instruments with the accelerator. After each run, JARVIS uploads all of the run parameters as well as any environmental monitoring to a run database based on the AirTable framework. JARVIS then manages the reconstruction and merging of the various datastreams using distributed computing resources at the Fermilab LHC Physics Center (LPC).

3.4. Fermilab beta source experiment

The beta source measurements were performed using a Ruthenium-106 source with an activity of approximately 1.3 mCi, and a typical beta energy of 1–2 MeV. The beta source is stored inside a brass "beta gun" collimator and mounted on a stand facing the sensor. All of the beta source measurements shown in this paper use the UCSC board described in Section 3.1, with a 1.3 mm hole drilled underneath the sensor to facilitate the passage of the beta rays. To reject events where the beta particle scatters inside the sensor, a tungsten shield with a 1.5 mm pinhole is mounted on the backside of the cooling block, about 2 cm behind the sensor. Particles that pass through the pinhole then reach the MCP-PMT, which serves both as the trigger and timing reference. By selecting beta rays that pass through the LGAD sensor, the pinhole, and the MCP-PMT, the resulting population of events have a uniform path length as well a MIP-like distribution of energy deposition in the sensor, as will be demonstrated in Section 5.1. Although the rate of beta rays that leave large, non-MIP charge deposits is significant in general, these events do not reach the MCP-PMT and are efficiently rejected. Photos of the beta source setup can be seen in Fig. 5.

4. Test beam results

The HPK 3.1 4x4 multi-pad sensor described in Section 2, mounted on the 16-channel readout board described in Section 3.1 was exposed to the beam to study the response of the sensor to minimum ionizing particles. Fig. 6 shows example signal amplitude and time of arrival distributions collected from protons passing through a single pad of the array.

We further present studies of the signal response across the entire area of the sensor, using the FTBF tracker to determine the location of the proton in each event. For these studies, a good quality track from the FTBF tracker is required, including hits in the final strip planes behind the sensor in order to reject protons that are deflected in material along the beamline.

The hit efficiency across the surface of the sensor is shown in Fig. 7. For a given position on the sensor, the efficiency is defined as the fraction of events with a signal amplitude larger than 40 mV out of all events with a high-quality track pointing through that position. This threshold is significantly larger than the noise and corresponds to a selection efficiency greater than 99% in all active regions. The isolated hits outside the sensor area arise due to events with misreconstructed trajectories or with more than one proton. In this figure, the inter-pad gap regions are clearly visible.

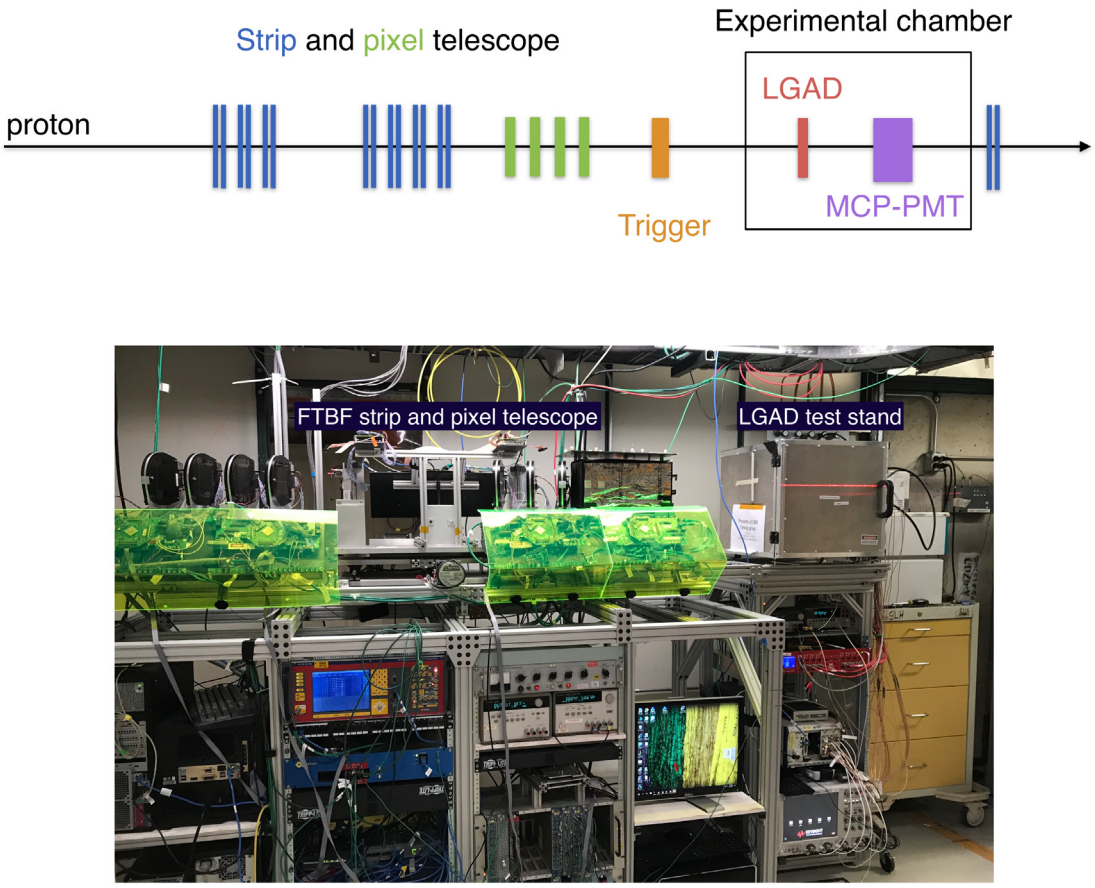

Fig. 4. A schematic diagram of the test beam setup and FTBF telescope geometry (top). A photo of the experimental setup and the telescope tracker at FTBF.

Fig. 8 shows a map of typical signal amplitudes observed across the surface of the sensor. The most probable amplitudes are extracted from a fit to the amplitude distribution using a Landau distribution convolved with a Gaussian distribution. The response is highly uniform, with pad-to-pad variations up to 10%, consistent with the variations in gain between different amplifiers on the readout board.

Fig. 9 shows a map of time resolution across the sensor. The time resolution is extracted as the width of a gaussian fit to the distribution of time difference between the LGAD and MCP-PMT timestamps for all events with a high-quality track at a given position on the sensor. The timestamps for each event are calculated by applying a 20% (40% for MCP-PMT) constant fraction discriminator to a linear fit on the rising edge of each waveform between 10% and 90% of the maximum amplitude. The time resolution is observed to be uniform for all of the active areas of the pads. Some bins are left empty due to insufficient event counts for performing a reliable fit to the distribution of time difference.

On the 16-channel FNAL board, the time resolution at high bias voltage reaches 40 ps, as shown in Fig. 9. However, the same sensor on the lower noise UCSC board reaches a resolution of 30 ps. This difference is due to slightly higher noise on the 16-channel board. Considering both measurements, we conclude that the intrinsic sensor resolution is 30 ps uniformly across the surface.

The map of the measured signal arrival times is shown in Fig. 10. Due to variation in path length of the channels on the 16-channel board, there are different time offsets for each pad. It was observed in a previous HPK sensor production [6] that a slight time offset exists within a single pad around the metalized bonding tab, shown in Fig. 2. To measure the same feature in the HPK 3.1 sensor production, we corrected the path-length offsets in each channel, and geometrically overlaid the signal arrival time measurements to visually enhance the feature around the bonding tab in Fig. 11. After this alignment, it is clear that the signals arising from protons passing underneath the metalized tab arrive approximately 20 ps earlier than other signals. The underlying cause for this feature is not entirely understood, but since the CMS and ATLAS timing detectors will use fully-metalized sensors, the time difference between metalized and non-metalized regions will not be relevant. Nonetheless, it is an interesting feature to monitor in future studies of sensors with limited surface metalization.

The studies shown above demonstrate for the first time the operation of a large area, multi-pad LGAD sensor exposed to a particle beam. We observe a high degree of uniformity of signal amplitude and time resolution across the sensor surface and reliable operation over a period of several days.

Additionally, several similar sensors were studied with a variation in inter-pad gap width. Fig. 12 shows 1D projections of the hit efficiency in the immediate vicinity of the inter-pad gaps. Each efficiency distribution is fit to a function which is a convolution of a step function representing the true efficiency, and a gaussian representing smearing from the tracker spatial resolution. The inter-pad gap is then defined as the distance between positions of 50% efficiency on each fit function. The resulting inter-pad gaps are found to be consistent with the values obtained from laser TCT measurements performed previously [15]. This demonstrates that inter-pad gaps measured using the benchtop laser are consistent with the inter-pad gaps measured with signals induced by particles as well. It is an important conclusion, as the benchtop measurements are generally easier to perform and have higher precision than can be achieved with the test beam.

5. Beta source characterization campaign

The beta source setup allows for much higher volume testing than is possible at the test beam. In this campaign, 22 HPK 3.1 sensors (as

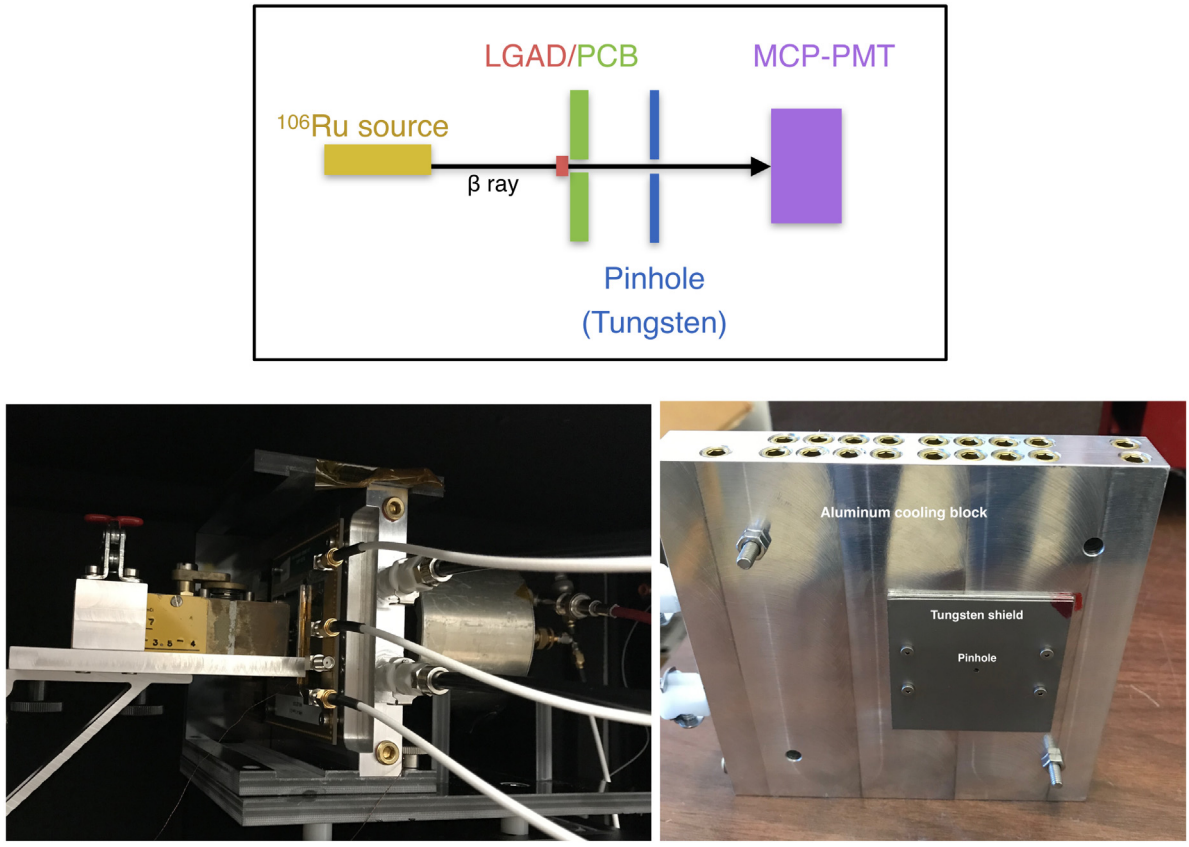

Fig. 5. A schematic diagram of the FNAL beta source setup (top). Photo of the beta source setup, showing the beta gun, the LGAD readout board mounted on cooling block, and the MCP-PMT (bottom left). Backside of the cooling block with tungsten pinhole attached (bottom right).

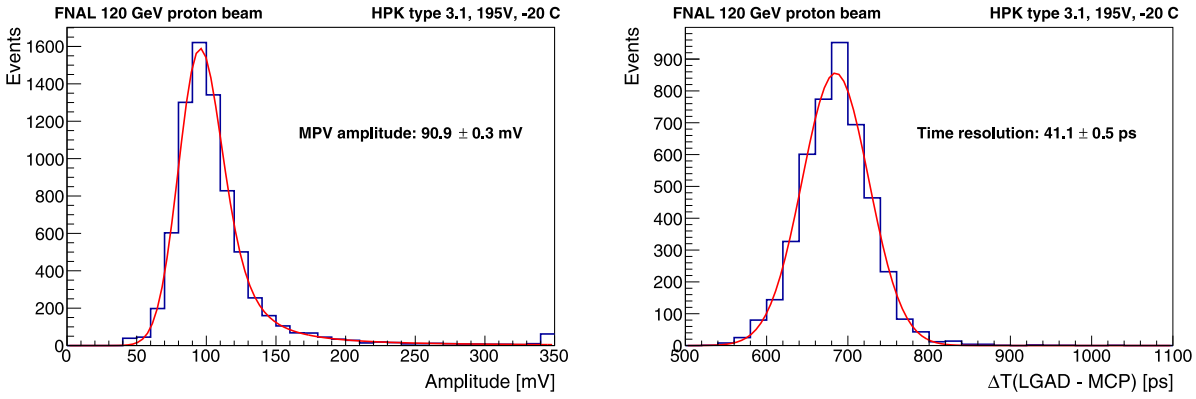

Fig. 6. Distributions from a single LGAD pad of the signal amplitude (left) and time of arrival difference with respect to the MCT-PMT (right). The amplitude distribution is fit with a Landau distribution convolved with a Gaussian to extract the most probable value. The time difference distribution is fit with a Gaussian function to extract the time resolution.

described in Section 2) were characterized with the beta source. One pad on each sensor was read out using the UCSC board. Each sensor was subjected to a bias voltage scan in increments of 5 V up to between 5 V to 10 V less than the breakdown voltage. At each bias voltage point, a few thousand events are acquired, and the entire process takes approximately one day to complete. A representative event collected using the beta source is shown in Fig. 13, including both the LGAD and MCP-PMT waveforms.

5.1. Comparison of beta particle and proton response

For the applications in CMS and ATLAS, the LGAD response to minimum ionizing particles (MIP) is the primary concern. Beta particles with 1 MeV energy are minimally ionizing for passage through small amounts of material [16]. As a first step to commission the beta source setup, we assess how well the signals arising from beta particles correspond with those from MIPs in the test beam. For this demonstration, we studied one sensor in an identical configuration using both the beta source and the 120 GeV proton beam. The distributions of charge and arrival time for a bias voltage of 170 V are shown in Fig. 14, and their evolution as a function of bias voltage is shown in Fig. 15. For a sense of scale, the most probable charge expected from a 50 μm sensor with no gain would be about 0.66 fC. Thus a sensor operating with a most probable signal of 20 fC indicates a gain of approximately 30.

The charge depositions and signal shapes originating from the two signal types are in remarkably good agreement, which indicates that

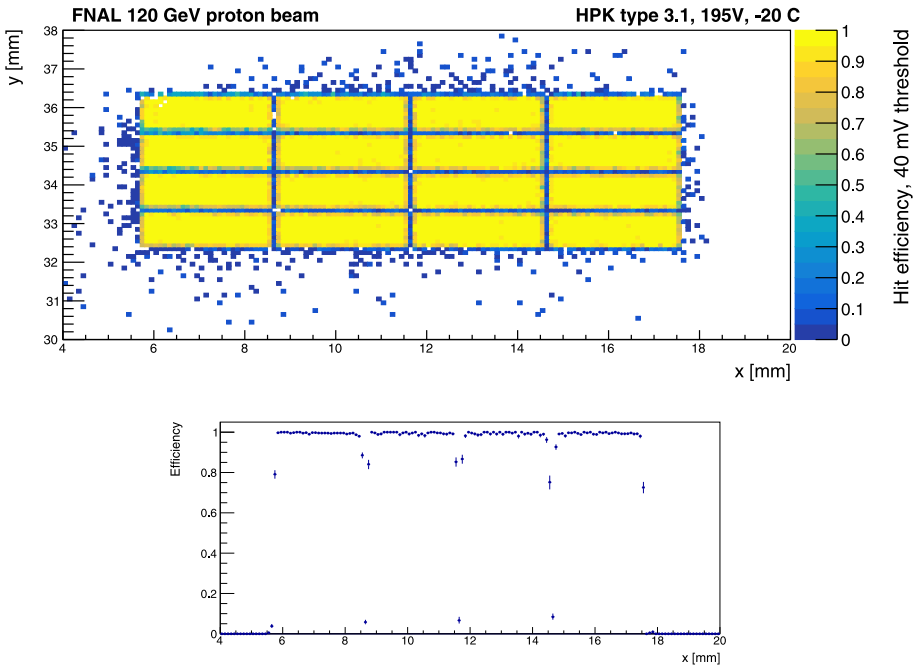

Fig. 7. Hit efficiency across surface of the 4x4 sensor for a threshold of 40 mV (top). Projection of the efficiency along the x-axis for the second row of pads, averaging over the region $33.6 < y < 34$ mm (bottom).

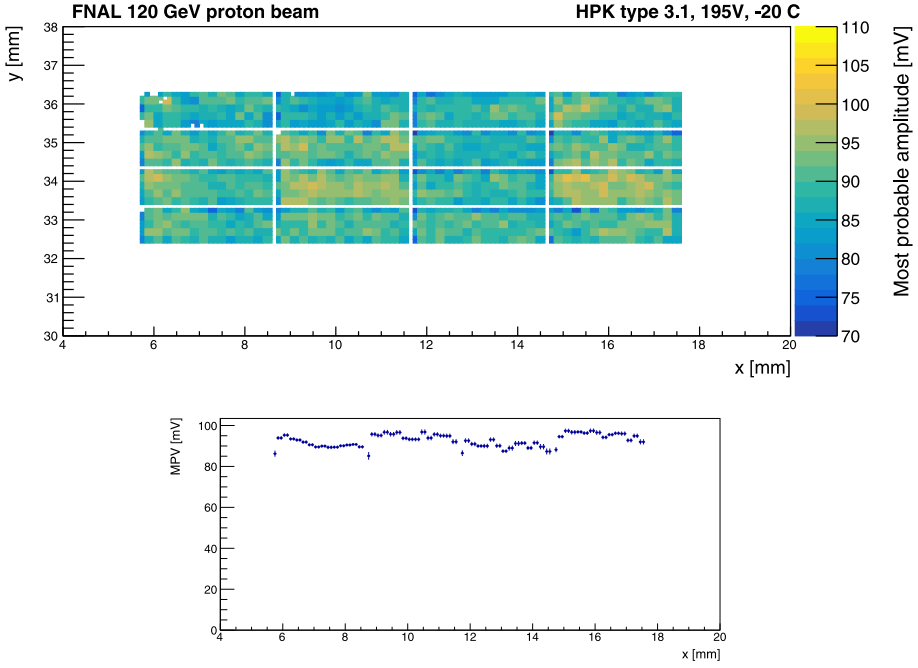

Fig. 8. Most probable signal amplitude across the surface of the 4x4 sensor (top). Projection of the most probable amplitude along the x-axis for the second row of pads, averaging over the region $33.6 < y < 34$ mm (bottom). Low efficiency regions between pads are not shown.

the selected beta events do represent a population of minimum ionizing particles. As previously described, the requirement that the beta particles pass in a straight path through the pinhole and reach the MCP-PMT reference detector ensures that particles experiencing larger energy loss or a hard scatter are excluded.

Although the LGAD signal properties match very well between the beta source and proton datasets, it can be seen in Figs. 14 and 15 that the resolutions measured from the beta source dataset is consistently larger by about 15 ps in quadrature. This degradation is due to two factors: the reduced response of the MCP-PMT reference to beta particles, and variations in path length (time of flight) that are present in the beta setup but not the test beam. A 15 ps contribution is subtracted in quadrature from all subsequent resolution measurements in order to isolate the resolution of the LGAD detector.

5.2. Relative calibration of readout boards

To efficiently characterize a large population of sensors, we employed multiple copies of the UCSC readout board to enable mounting and wirebonding sensors in batches. It is then important to establish that all readout boards give uniform results. Before the campaign began, a single calibration LGAD was cycled through all candidate

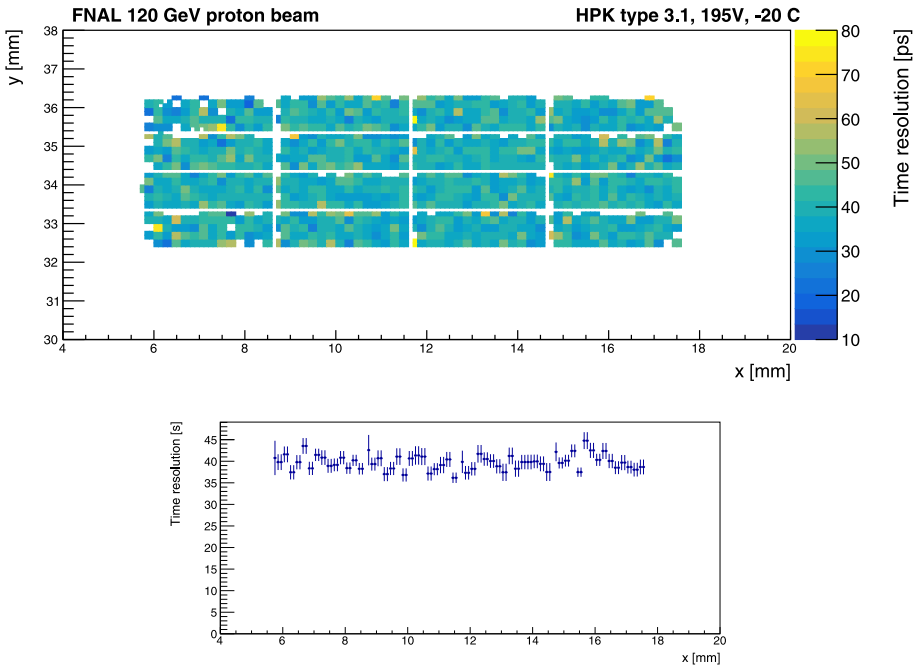

Fig. 9. Time resolution across surface of the 4x4 sensor (top). Projections of the resolution vs x for the second row of pads, averaging over the region $33.6 < y < 34$ mm (bottom). Low efficiency regions between pads are not shown.

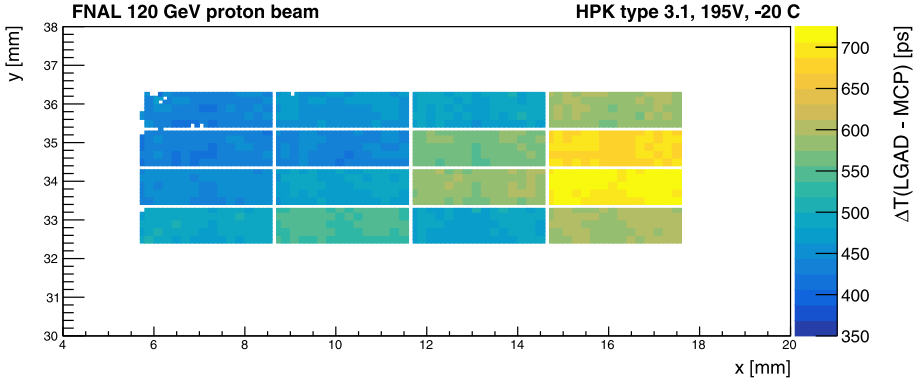

Fig. 10. LGAD signal arrival time with respect to the MCP-PMT timestamp across the surface of the 4x4 sensor. Low efficiency regions between pads are not shown.

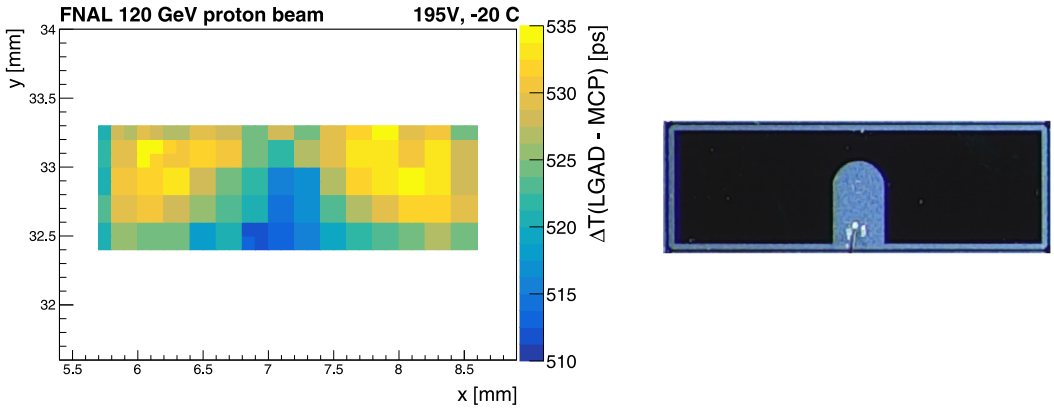

Fig. 11. Average arrival time across a single pad after correcting for offsets in individual channels on the readout board, overlaying and averaging all pads together (left). Image of single pad from the 4x4 sensor, illustrating the metalized tab (right).

readout boards to gauge the board uniformity. All four of the UCSC readout boards used in this campaign reproduced essentially identical results, as can be seen in Fig. 16. The remarkable reproducibility of the results demonstrates the excellent environmental control in the

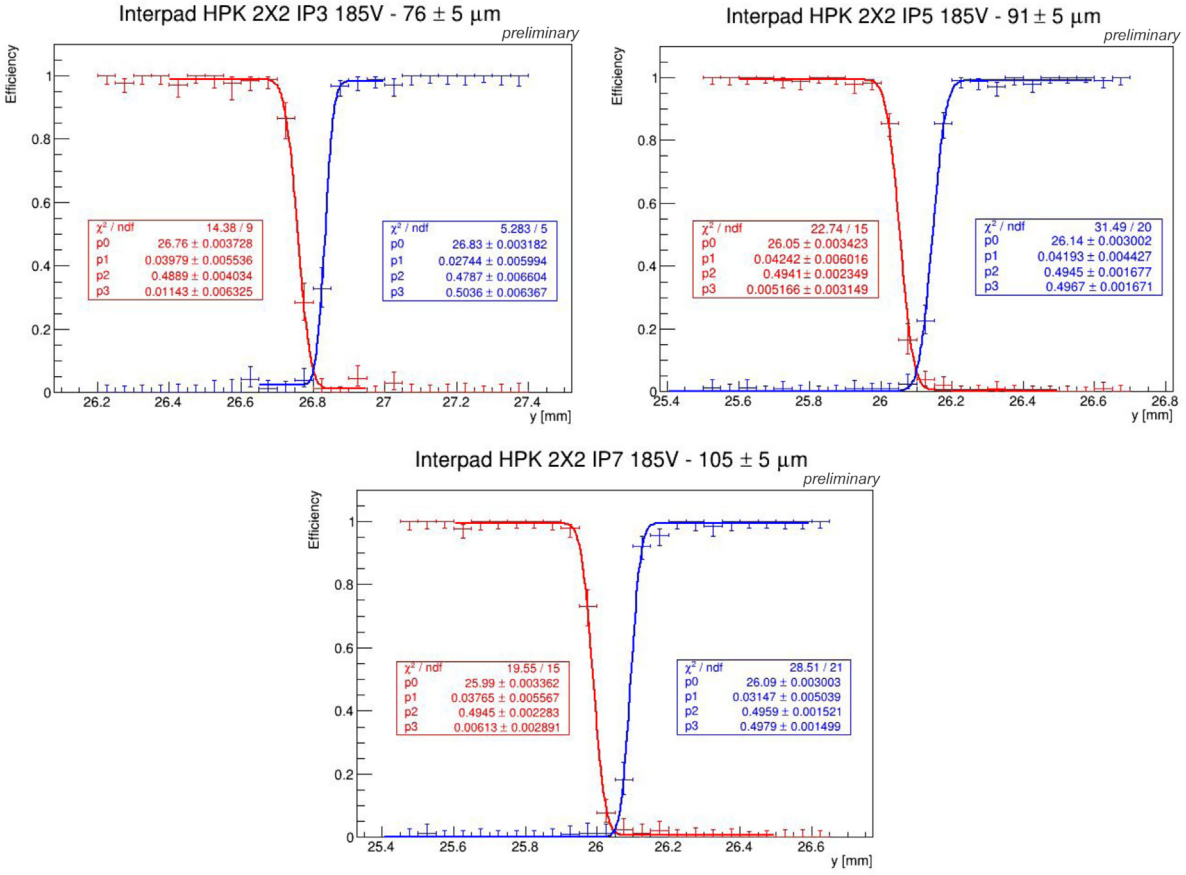

Fig. 12. Measurement of the inter-pad gap in three different sensors. Top left: nominal gap 30 µm; measured 76 ± 5 µm. Top right: nominal gap 50 µm; measured 91 ± 5 µm. Bottom: nominal gap 70 µm; measured 105 ± 5 µm.

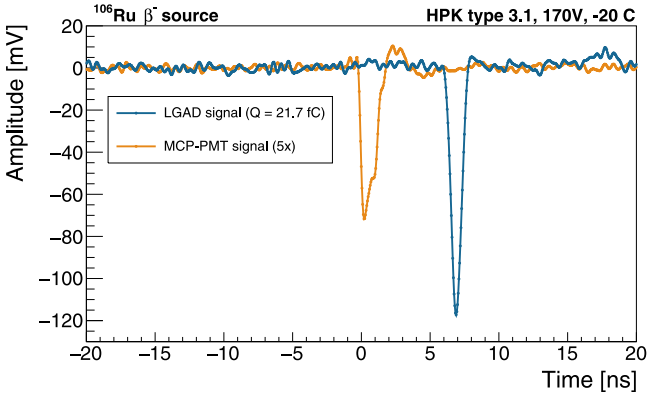

Fig. 13. Waveforms from the LGAD and MCP-PMT in a representative event, sampled at 20 GS/s. The MCP-PMT waveform is scaled vertically by a factor of 5 for better visibility. The LGAD waveform shown is from the sensor with $1 \times 3\,\text{mm}^2$ pads, at wafer position P2 with a nominal inter-pad gap of 50 µm (see Table 1). The collected charge observed in this event is 21.7 fC, very close to the most probable value for this sensor (see distributions in Fig. 14).

beta setup and builds confidence that even small differences observed between sensors are meaningful.

5.3. Beta source results

The results of the beta measurement campaign are shown in Figs. 17 to 20. Figs. 17 and 18 show the charge collection as a function of bias voltage for the sensors of pad size $1 \times 3\,\text{mm}^2$ and $1.3 \times 1.3\,\text{mm}^2$. Variation in the gain layer concentration between sensors results in a translation of these curves along the bias voltage axis, with the key figure of merit being the bias voltage to reach a certain charge threshold. Among the $1 \times 3\,\text{mm}^2$ sensors, there is a correlation with the turn-on of the charge curve and the position of the sensor on the wafer. Sensors near the center of the wafer (P1–P2) require a bias voltage approximately 10 V larger to reach the same gain as sensors towards the edge of the wafer (P3–P5). The wafer positions of the $1.3 \times 1.3\,\text{mm}^2$ sensors were not preserved, but a similar scale of variation in bias voltage of 10–15V is observed to reach a given gain value. These differences represent slight variation in the concentration of the gain implant.

Fig. 19 shows the risetime and time resolution for each LGAD as a function of the collected charge at each bias point. There are two groups observed in the risetime distribution, corresponding to pads with $1.3 \times 1.3\,\text{mm}^2$ and $1 \times 3\,\text{mm}^2$ areas. The $1.3 \times 1.3\,\text{mm}^2$ pads reach 460 ps and $1 \times 3\,\text{mm}^2$ pads reach 500 ps risetimes. This difference is expected due to the different capacitances introduced by each pad size. The faster risetime yields improves the time resolution at low charge, but when operated at high gain, both pad sizes converge to an asymptotic time resolution of 25–30ps. Within each of the two sensor populations, the relationship between collected charge and either risetime or time resolution is common to all sensors. The small differences in operating voltage, visible in Figs. 17 and 18, have limited impact on timing performance at any given charge. There is a small effect from the difference in operating voltage: sensors with a larger operating voltage have risetime that is about 10 ps faster than sensors with a lower operating voltage. This can be seen by comparing the P2 (orange) sensors against the P4 (green) sensors in Figs. 17 and 19 (left). This stems from the fact that electron drift velocity is not yet saturated

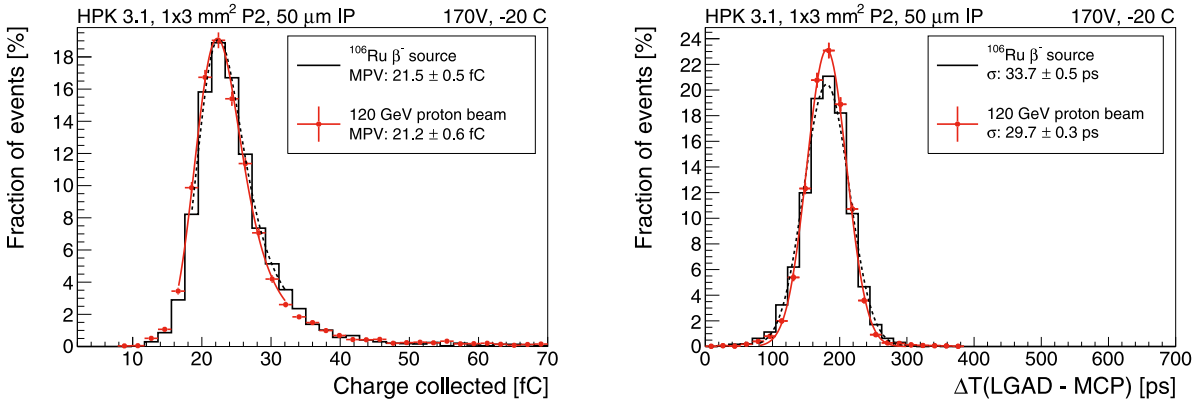

Fig. 14. Distributions of collected charge (left) and arrival time difference (right) observed from a single sensor exposed to the test beam and the beta source. This sensor has a pad size of $1 \times 3\,\mathrm{mm}^2$, is from wafer position P2, and has a nominal inter-pad gap of 50 µm. It was operated at a bias voltage of 170 V and a temperature of −20 C. The legends indicate the most probable values of the collected charge, and the width of the ΔT distributions. The width includes contributions from the LGAD resolution as well as the MCP-PMT reference.

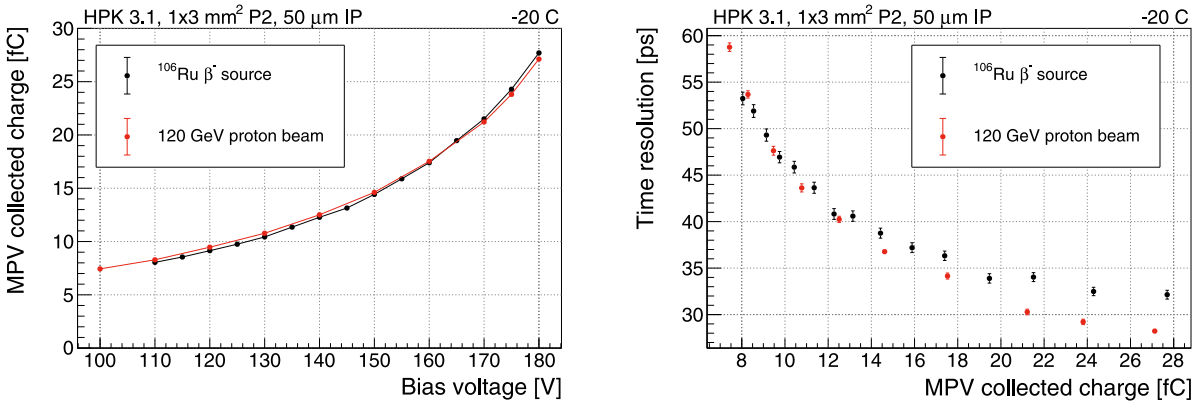

Fig. 15. Comparison of the collected charge (left) and time resolution (right) observed using the test beam and the beta source for a sequence of measurements with varying bias voltage. Each point corresponds to a single bias voltage. The measurements with a bias voltage of 170 V and near 21 fC correspond to the distributions shown in Fig. 14. The time resolutions shown includes both the LGAD and MCP-PMT contributions. The small difference observed at very high charge is used to estimate the additional resolution contribution present in the beta source setup.

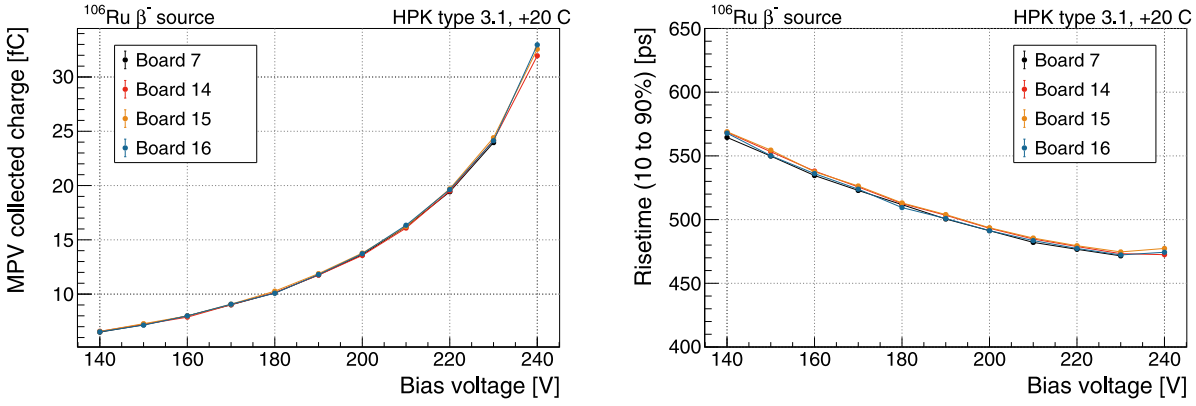

Fig. 16. Comparison of the four UCSC readout boards used for the beta source characterization campaign. All four show good uniformity in charge (left) and risetime (right) for a single sensor rotated through all four boards.

until the highest bias voltages, and so the sensors with higher operating voltages are closer to velocity saturation at a given gain.

As can be seen in Fig. 19, a charge collection of 20 fC is sufficient to provide 30 ps or better time resolution. We define the voltage where 20 fC charge collection is achieved to be the minimum operating voltage of each sensor. Furthermore, from Fig. 17, we see that the sensor can still be operated with a bias up to about 20 V above the minimum operating voltage, before entering breakdown region. Therefore, each sensor has a roughly 20 V bias voltage range for operation with better than 30 ps time resolution. We note that these observations should be applied only to non-irradiated sensors.

Sensors were studied with variation in inter-pad gap size, and both with and without surface metalization. We observe that neither of these properties have a significant effect on any aspect of the performance, as can be seen in Figs. 17 and 19.

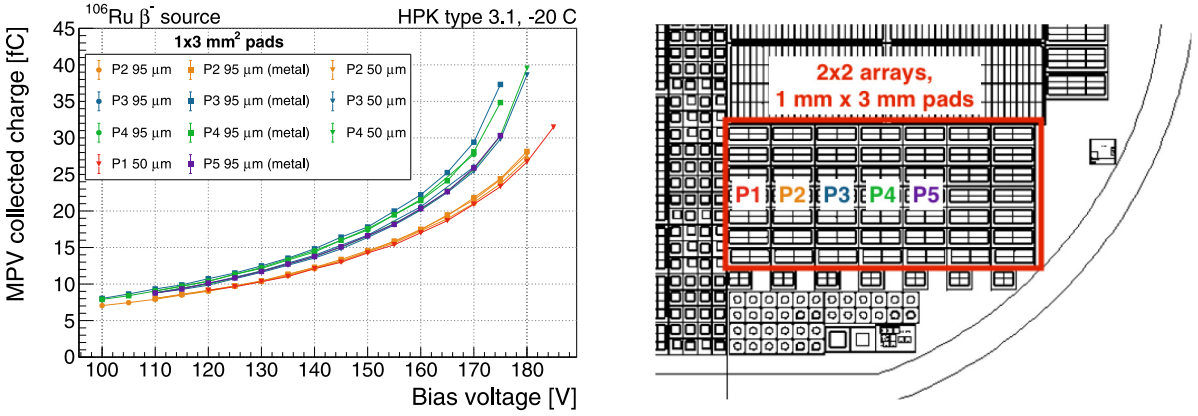

Fig. 17. Collected charge as a function of bias for the sensors with $1 \times 3\,\mathrm{mm}^2$ pads (left). The legend indicates the nominal inter-pad gap values, whether the surface is fully metalized, the position on the wafer (P1–P5). The right panel shows a portion of the wafer layout from Fig. 1 that indicates the locations of columns P1–P5. The pads near the center of the wafer (P1–P2) need an additional 10 V to deliver the same charge as the sensors from the edge of the wafer (P3–P5). (For interpretation of the references to color in this figure legend, the reader is referred to the web version of this article.)

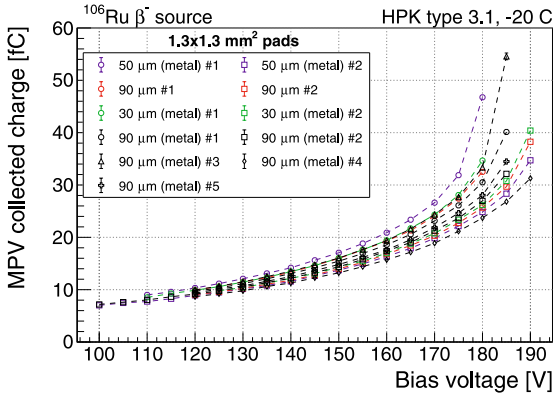

Fig. 18. Collected charge as a function of bias for the sensors with $1.3 \times 1.3\,\mathrm{mm}^2$ pads (right). The legend indicates the nominal inter-pad gap values, whether the surface is fully metalized.

5.4. Correspondence with probe CV measurements

A key challenge for the operation of a large scale timing detector is to ensure all pads on each sensor can reach the gain needed to achieve the required time resolution with all pads constrained to operate at the same bias voltage. Due to the long duration and complexity of the measurement, it is not possible to characterize each sensor fully using the beta source telescope during the construction phase of the detector. However, characterization of sensors with a probe station is a practical alternative for sensor quality assurance. Therefore establishing the relationship between charge collection and the probe station measurements allows for efficient LGAD sensor quality control and characterization of uniformity. With the goal of establishing that relationship, the 22 sensors included in this campaign were characterized using a probe station in the Torino UFSD lab [17].

Probe station CV measurements can be used to determine the depletion voltage of the gain layer, which indicates the integrated concentration of the gain layer dopant. The CV curves for all 22 sensors are shown in Fig. 20 (left). Sensors which require a larger voltage to deplete the gain layer should have a larger gain at a given bias voltage. To quantify the variation in the depletion voltage of the gain layer, we define a CV transition voltage where the capacitance

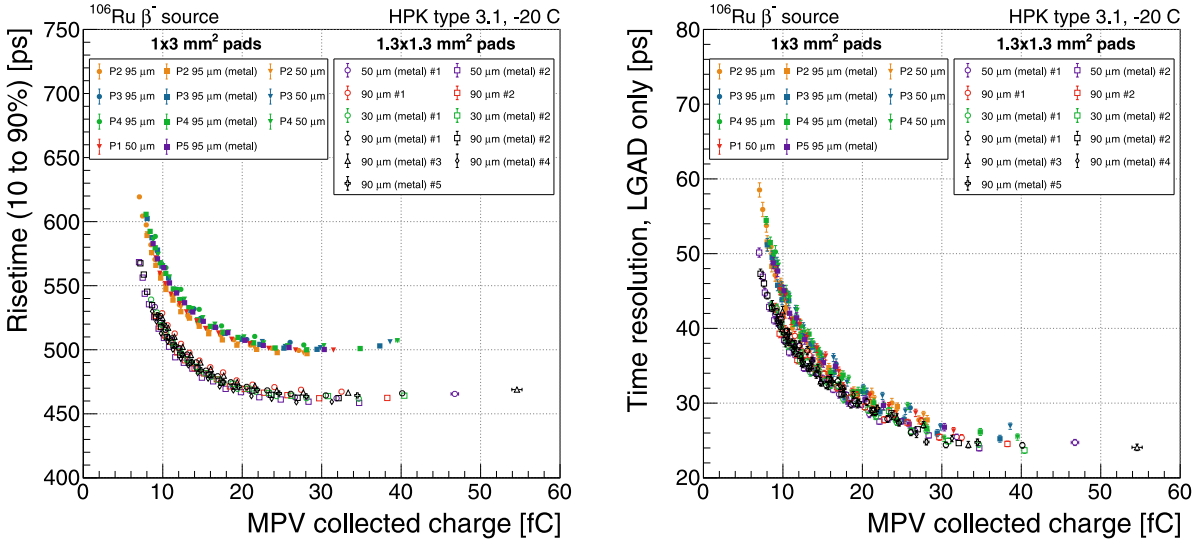

Fig. 19. Risetime and time resolution for the 22 sensors as a function of the collected charge at each bias voltage. The $1 \times 3\,\mathrm{mm}^2$ pads have a slightly slower risetime due to the larger capacitance, but similar asymptotic time resolution at high values of charge. The time resolution values shown have been corrected to remove the MCP-PMT contribution of 15 ps. (For interpretation of the references to color in this figure legend, the reader is referred to the web version of this article.)

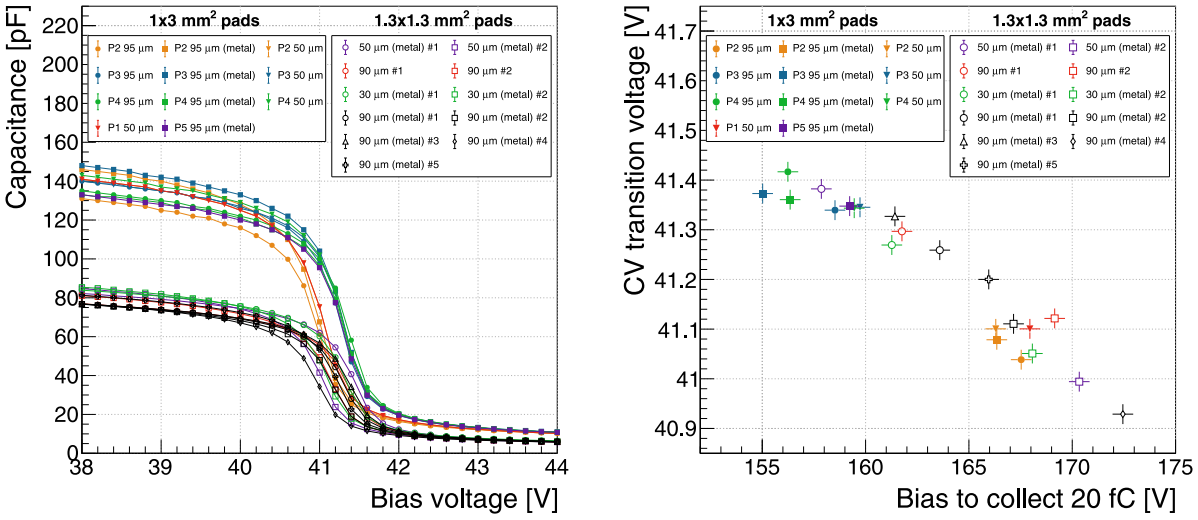

Fig. 20. Capacitance–voltage curve for the 22 sensors, measured with probe station (left). Correlation of the CV transition voltage of each sensor with the bias voltage to collect 20 fC (right).

crosses a particular threshold: 75 pF (52 pF) for $1 \times 3\,\text{mm}^2$ ($1.3 \times 1.3\,\text{mm}^2$) pad sensors. These capacitance thresholds correspond to roughly the midpoint of the steeply falling portions of each curve.

We study the relationship between the CV transition voltage and the operating voltage of each sensor. As was observed in Section 5.3, a collected charge of 20 fC ensures 30 ps or better time resolution for the sensors produced. The operating voltage is taken to be the bias voltage at which the MPV of the collected charge reaches 20 fC. In Fig. 20 (right) we show the CV transition voltage versus the operating voltage for each of the sensors studied, where we observe a near linear relationship with few outliers. Therefore, it is possible to predict the operating voltage to within a few volts based on the measured CV transition voltage. This ability will be a crucial tool for designing the bias voltage distribution scheme and performing sensor quality control during the production of the ATLAS and CMS timing detectors.

For reliable operation of a large sensor, the pad with the smallest gain must reach the desired operating gain at a bias voltage less than the breakdown voltage of the pad with the largest gain. For the HPK type 3.1 batch, the difference between the operational bias voltage and the breakdown voltage is approximately 20 V as seen in Fig. 17. Furthermore, based on Fig. 20, all pads can reach the desired gain within a 20 V interval as long as the variation in the CV transition voltage is within approximately 1% (the full range in the y-axis).

Probe station measurements have been previously reported over the scale of entire wafers that were part of this LGAD production [18]. The variation in the gain layer depletion voltage has been observed to be on the order of a few percent on distance scales across an entire wafer. However, in regions limited to the size of a single sensor for CMS and ATLAS (about $2 \times 4\,\text{cm}^2$), the variation is limited to roughly 1%. The results presented here shows that this magnitude of gain variation would allow all pads on a full sized sensor to be operated with better than 30 ps resolution even when constrained to a single bias voltage. We conclude that the gain layer uniformity achieved in HPK type 3.1 production batch would be sufficient to provide working full-sized sensors for CMS and ATLAS.

6. Conclusion

We report comprehensive studies of HPK type 3.1 LGAD prototypes for the CMS and ATLAS timing detectors, including testbeam, beta source, and probe station measurements. Through careful design of each measurement campaign, we have been able to correlate the results from each measurement significantly expand the value of each technique. By comparing to testbeam measurements, we successfully validated the accuracy of the beta source measurements, which enables us to survey a much larger volume of sensors. Careful subsequent comparisons with probe station measurements allowed us to translate the impact of subtle variations in the gain layer doping concentration to quantitative variations in operating voltage. Ultimately this collection of measurements yields the possibility for detailed assessment of LGAD productions relying only on simple probe station measurements.

The uniformity observed in the HPK 3.1 LGAD production is sufficient to produce working, full-sized sensors for CMS and ATLAS. Sensors from this production achieve 30 ps resolution when operated in a 20 V bias voltage interval that provides a collected charge of at least 20 fC. Probe station measurements across wafers from this production indicate adequate gain uniformity such that regions separated by 2 cm to 4 cm have compatible operating bias voltages. This conclusion addresses one of the two critical questions facing the sensors for these timing detectors. The remaining question is to demonstrate that the LGAD sensors have sufficient radiation tolerance to survive until the end of the life of the HL-LHC, or a fluence up to $1.5 \times 10^{15}\,\text{neq/cm}^2$ for the inner radius of CMS. The thoroughly characterized HPK 3.1 LGAD sensors documented in this paper provide an excellent sample for robust measurements of the radiation hardness with high statistics.

Declaration of competing interest

The authors declare that they have no known competing financial interests or personal relationships that could have appeared to influence the work reported in this paper.

Acknowledgment

We thank the Fermilab accelerator's team for very good beam conditions during our test beam time. We thank Mandy Kiburg, Evan Niner, Todd Nebel, Jim Wish, and all of the FTBF personnel for their support during the test beam experiments. We would like to thank Lorenzo Uplegger, Alan Prosser and Ryan Rivera for their critical role in establishing the FTBF tracker and its DAQ and trigger chain. We are grateful for the technical support of the Fermilab SiDet department, especially Bert Gonzalez and Michelle Jonas for the rapid production of wire-bonded and packaged LGAD assemblies, and Abhishek Bakshi for the mechanical design of the experimental structures. This document was prepared using the resources of the Fermi National Accelerator Laboratory (Fermilab), a U.S. Department of Energy, Office of Science, HEP User Facility. Fermilab is managed by Fermi Research Alliance, LLC (FRA), acting under Contract No. DE-AC02-07CH11359. Part of

this work was performed within the framework of the CERN RD50 collaboration.

This work was supported by the Fermilab LDRD 2017.027; by the United States Department of Energy grant DE-FG02-04ER41286; by the California Institute of Technology High Energy Physics under Contract DE-SC0011925; by the European Union's Horizon 2020 Research and Innovation funding program, under Grant Agreement no. 654168 (AIDA-2020) and Grant Agreement no. 669529 (ERC UFSD669529); by the Italian Ministero degli Affari Esteri and INFN Gruppo Vl; and by the National Research Foundation of Korea (NRF) grant funded by the Korea government (MSIT) (Grants No. 2018R1A6A1A06024970, No. 2020R1A2C1012322 and Contract NRF-2008-00460).

References

[1] G. Apollinari, O. Brüning, T. Nakamoto, L. Rossi, Chapter 1: High Luminosity Large Hadron Collider HL-LHC. High Luminosity Large Hadron Collider HL-LHC, CERN Yellow Report, 2017, pp. 1–19, 21 p.

[2] D. Schulte, FCC-hh design highlights, ICFA Beam Dyn. Newslett. 72 (2017) 99–109.

[3] CMS Collaboration, A MIP Timing Detector for the CMS Phase-2 Upgrade, Tech. Rep. CERN-LHCC-2019-003. CMS-TDR-02, CERN, Geneva, 2019.

[4] N. Cartiglia, A. Staiano, V. Sola, et al., Beam test results of a 16 ps timing system based on ultra-fast silicon detectors, Nucl. Instrum. Methods A 850 (2017) 83–88.

[5] G. Pellegrini, P. Fernandez-Martinez, M. Baselga, et al., Technology developments and first measurements of Low Gain Avalanche Detectors (LGAD) for high energy physics applications, Nucl. Instrum. Methods A 765 (2014) 12–16.

[6] A. Apresyan, S. Xie, C. Pena, et al., Studies of uniformity of 50 μm low-gain avalanche detectors at the Fermilab test beam, Nucl. Instrum. Methods A 895 (2018) 158–172.

[7] Y. Jin, H. Ren, S. Christie, et al., Experimental study of acceptor removal in UFSD, Nucl. Instrum. Methods A 983 (2020) 164611.

[8] http://www.photek.com/pdf/datasheets/detectors/DS006_Photomultipliers.pdf.

[9] https://www.keysight.com/en/pd-2233037-pn-MSOX92004A/infiniium-high-performance-oscilloscope-20-ghz.

[10] http://ftbf.fnal.gov.

[11] S. Kwan, C. Lei, D. Menasce, et al., The pixel tracking telescope at the Fermilab Test Beam Facility, Nucl. Instrum. Methods A 811 (2016) 162–169.

[12] M. Turqueti, R.A. Rivera, A. Prosser, J. Andresen, J. Chramowicz, CAPTAN: A hardware architecture for integrated data acquisition, control, and analysis for detector development, in: 2008 IEEE Nuclear Science Symposium Conference Record, 2008, pp. 3546–3552.

[13] https://www.ni.com/en-us/support/model.pxi-2596.html.

[14] https://github.com/CMS-MTD/JARVIS.

[15] S. Bharthuar, J. Ott, K. Helariutta, et al., Study of interpad-gap of HPK 3.1 production LGADs with transient current technique, Nucl. Instrum. Methods A 979 (2020) 164494.

[16] M. Tanabashi, et al., Particle Data Group Collaboration, Review of particle physics, Phys. Rev. D 98 (2018).

[17] V. Sola, R. Arcidiacono, N. Cartiglia, et al., Characterisation of 50 μm thick LGAD manufactured by FBK and HPK, in: 14th "Trento" Workshop on Advanced Silicon Radiation Detectors FBK, Trento, 25–27 February 2019, 2019, https://cds.cern.ch/record/2667026.

[18] M. Ferrero, et al., Recent studies and characterization on UFSD sensors, in: 34th RD50 Workshop, Lancaster, UK, 2019.